

Inferring High-Order Couplings with Neural Networks

Aurélien Decelle

*Escuela Técnica Superior de Ingenieros Industriales, Universidad Politécnica de Madrid,
Calle de José Gutiérrez Abascal 2, Madrid 28006, Spain and
Departamento de Física Teórica, Universidad Complutense de Madrid, 28040 Madrid, Spain*

Alfonso de Jesús Navas Gómez* and Beatriz Seoane

Departamento de Física Teórica, Universidad Complutense de Madrid, 28040 Madrid, Spain

Maximum entropy methods, based on the inverse Ising/Potts problem from statistical mechanics, are essential for modeling interactions between pairs of variables in data-driven problems across disciplines such as bioinformatics, ecology, and neuroscience. Despite their considerable success, these methods typically fail to capture higher-order interactions that are often essential for understanding complex systems. Conversely, modern machine learning methods capture these complex interactions, but the computational cost of interpretable frameworks makes them impractical for real-world applications. Restricted Boltzmann Machines (RBMs) provide a computationally efficient way to capture statistical correlations using hidden nodes in a bipartite neural network. In this study, we introduce a new method that maps RBMs to generalized Potts models, allowing for the extraction of interactions up to any specified order. This method utilizes large- N approximations, enabled by the RBM's simple structure, to extract effective many-body couplings with minimal computational effort. Furthermore, we propose a robust framework for extracting higher-order interactions in more complex probabilistic models and a simple gauge-fixing method within the effective many-body Potts model. Our validation on synthetic datasets confirms the method's ability to recover two- and three-body interactions accurately. When applied to protein sequence data, the framework competently reconstructs protein contact maps and provides performance comparable to the best inverse Potts models. These findings confirm that RBMs are an effective and streamlined tool for exploring higher-order interactions within complex systems.

Introduction.— The Maximum Entropy (ME) principle in data-driven modeling consists of fitting empirical low-order moments of the data, such as means and covariances, while making minimal assumptions about unobserved variables. In the case of network inference with categorical variables, ME data modeling is formulated as an inverse Potts problem of statistical mechanics, i.e., we seek the fields and pairwise couplings of a Potts Hamiltonian that best describes the observed data. This approach is interpretable, easy to use, and provides meaningful insights even in situations with limited data. It has provided a framework [1] for understanding the underlying dynamics of many complex systems, including neural circuits [2–5], gene networks [6–8], protein structures [9–11], and ecosystems [12]. However, the expressiveness of pairwise models is inherently limited because they reduce all group interactions to pairwise terms, which precludes capturing the higher-order interactions crucial in real-world systems [13, 14]. On the other hand, although modern generative machine learning models have recently achieved significant breakthroughs, such as predicting protein structures from sequences [15, 16], they often struggle in data-scarce scenarios and lack interpretability. Furthermore, extracting meaningful and understandable insights from their parameters remains challenging, with significant ongoing efforts [17–20].

An alternative that effectively mediates between simple pairwise modeling and modern deep learning frameworks is the Restricted Boltzmann Machine (RBM) [21]. In contrast to traditional pairwise models, an RBM works on a bipartite graph in which only one layer describes the observable data. Introducing latent or hidden variables allows RBMs to act as universal approximators [22] and significantly increases their expressive power while keeping the number of parameters to be learned under control. Recent studies have shown that binary RBMs can be reinterpreted as a generalized Ising or lattice gas model with interactions that go beyond pairwise to include higher-order terms [23–26]. Furthermore, this mapping has proven useful for inference applications, as it enables the extraction of coupling parameters from simulated data with multi-body interactions using equal or fewer parameters than analogous inverse Ising models [26]. This highlights the superior ability of RBMs to model complex systems, offering enhanced performance over standard maximum entropy techniques without additional computational costs and providing practical techniques to assess the explainability of such models [27].

Most applications of ME focus on categorical variables rather than binary ones. A prominent example is Direct Coupling Analysis (DCA) [9, 10], which uses inverse Potts models to infer epistatic couplings from the Multiple Sequence Alignment (MSA) of protein [11] or RNA families [28]. MSAs align sequences from homologous families—groups of proteins or RNAs with a common evolutionary ancestor—to identify conserved regions, re-

* alfonn01@ucm.es

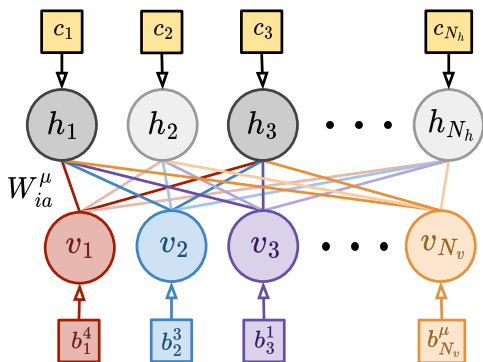


FIG. 1. **Diagram of the Potts-Bernoulli RBM.** Hidden variables h_a can take only two possible values, while visible variables v_i take on q different states or colors.

vealing structural, functional, and evolutionary relationships. Recent studies introduced methods to identify the closest pairwise model distribution to a trained probabilistic model, enabling the extraction of effective pairwise couplings from modern neural networks [18, 29], including RBMs [29]. However, these approaches are computationally intensive, requiring either averaging over numerous single-site data permutations or performing sampling, which limits their applicability to pairwise interactions. In this work, we propose a generic theoretical expression to infer n -th order couplings from generic categorical probabilistic models and introduce a fast, reliable framework to approximate high-order couplings in Potts RBMs, leveraging their straightforward energy function structure for approximations. We show that the derived expressions accurately infer pairwise and three-wise couplings in controlled experiments and enable protein contact predictions from trained RBMs with accuracy comparable to state-of-the-art DCA methods.

The Potts-Bernoulli RBM.— Consider an undirected stochastic neural network defined on a bipartite lattice (see Fig. 1), a visible layer $\mathbf{v} = \{v_i\}_{i=1}^{N_v}$, which represents the data, and a hidden layer $\mathbf{h} = \{h_a\}_{a=1}^{N_h}$, which encodes the interactions among the visible variables. As in other energy-based generative models, the joint probability of any given configuration $\{\mathbf{v}, \mathbf{h}\}$ is given by the Boltzmann distribution

$$p(\mathbf{v}, \mathbf{h}) = \frac{1}{\mathcal{Z}} e^{-\mathcal{H}(\mathbf{v}, \mathbf{h})}, \quad \text{where } \mathcal{Z} = \sum_{\{\mathbf{v}, \mathbf{h}\}} e^{-\mathcal{H}(\mathbf{v}, \mathbf{h})}, \quad (1)$$

with $\mathcal{H}(\mathbf{v}, \mathbf{h})$ being the *energy function* or the *Hamiltonian* of the model. We define the hidden nodes as Bernoulli variables, i.e., $h_a \in \{0, 1\}$, and the visible nodes as categorical variables, or Potts “spins”, that can take on q states or colors, i.e., $v_i \in \{1, \dots, q\}$. Hence, the Hamiltonian of such a system is given by

$$\mathcal{H}(\mathbf{v}, \mathbf{h}) = - \sum_{i,a,\mu} W_{ia}^\mu h_a \delta_\mu^{v_i} - \sum_{i,\mu} b_i^\mu \delta_\mu^{v_i} - \sum_a c_a h_a, \quad (2)$$

where δ_i^j denote the Kronecker delta ($\delta_i^j = 1$ if $i = j$, and

$\delta_i^j = 0$ otherwise), and $\Theta \stackrel{\text{def}}{=} \{\mathbf{W}, \mathbf{b}, \mathbf{c}\}$ are the model parameters. The *weight tensor* $\mathbf{W} = \{W_{ia}^\mu\}$, is a rank-3 tensor that models the interactions between the visible and hidden layers, and the *visible* and *hidden biases*, denoted by $\mathbf{b} = \{b_i^\mu\}$ and $\mathbf{c} = \{c_a\}$, respectively, are local fields acting in a specific visible or hidden site in the lattice. For clarity, we use Latin indexes $i \in \{1, \dots, N_v\}$ and $a \in \{1, \dots, N_h\}$ to denote visible and hidden sites, respectively, and Greek ones $\mu \in \{1, \dots, q\}$ to indicate the possible colors of the visible variables.

The parameters of an RBM are typically trained through likelihood maximization to ensure that the marginal distribution over the visible units, $p(\mathbf{v}) = \sum_{\mathbf{h}} p(\mathbf{v}, \mathbf{h})$, closely matches the empirical distribution of a dataset $\mathcal{D} = \{\mathbf{v}^{(m)}\}_{m=1}^M$ containing M entries, i.e., $p_{\mathcal{D}}(\mathbf{v}) = \frac{1}{M} \sum_{m=1}^M \delta(\mathbf{v} - \mathbf{v}^{(m)})$, where δ represents the N_v -dimensional Dirac delta distribution. For details about the training process, see Appendix A.

It is easy to verify that the parameter transformation.

$$W_{ia}^\mu \rightarrow W_{ia}^\mu + A_{ia}, \quad b_i^\mu \rightarrow b_i^\mu + B_i, \quad c_a \rightarrow c_a - \sum_i A_{ia}$$

leaves the Boltzmann distribution in (1) unchanged. Such invariance is a natural consequence of the over-parametrization of Potts models [11, 29]. Fixing the model gauge is helpful in uniquely defining the inference problem and ensuring efficient convergence to optimal parameters during training. The most widely used gauges are the *lattice gas* gauge, which assumes

$$b_i^q = W_{ia}^q = 0, \quad \forall i, a, \quad (3)$$

and the *zero-sum* gauge, defined by

$$\sum_\mu \hat{b}_i^\mu = \sum_\mu \hat{W}_{ia}^\mu = 0, \quad \forall i, a. \quad (4)$$

Hereafter, we will use the “ $\hat{\cdot}$ ” (hat) symbol to refer to the couplings in their correspondingly zero-sum gauge. We did not observe any particular advantage or disadvantage in using either gauge during RBM training. For consistency, we employed the zero-sum gauge during the RBM training analyzed in our experiments as in [30].

Generalized multi-body Potts model.— The binary RBM is a universal approximator [22], capable of modeling any multivariate random variable over a binary vector space given sufficient hidden units. Thus, when the dataset comprises equilibrium configurations of a multi-body Ising Hamiltonian, RBM learning can capture interactions of any order among visible units, provided enough data is available. This theoretical property has been demonstrated in practice: recent studies [23–26] have shown that the energy function of a binary RBM can be precisely mapped to an effective Ising model with interactions of all orders, represented by coupling tensors dependent on the RBM parameters Θ .

Ref. [26] demonstrated that the mapping between RBMs and interacting physical models can accurately

reconstruct the underlying interactions, including three-body terms, used to generate synthetic data in controlled inverse experiments. Building on this foundation, we propose a theoretical and practical approach to map any categorical RBM onto a Potts Hamiltonian. We begin with the marginalized Hamiltonian of the Potts-Bernoulli RBM, obtained by summing over the hidden units, i.e., $p(\mathbf{v}) = \sum_{\mathbf{h}} p(\mathbf{v}, \mathbf{h}) \propto e^{-H(\mathbf{v})}$, which is given by

$$H(\mathbf{v}) = - \sum_{i,\mu} b_i^\mu \delta_\mu^{v_i} - \sum_a \ln \left(1 + e^{c_a + \sum_{i,\mu} W_{ia}^\mu \delta_\mu^{v_i}} \right), \quad (5)$$

where b_i^μ are the visible biases, c_a are the hidden biases, and W_{ia}^μ represents the interaction weights between visible and hidden units. and map it into an effective Potts Hamiltonian with multi-body interactions,

$$\mathcal{H}(\mathbf{v}) = - \sum_{i,\mu} H_i^\mu \delta_\mu^{v_i} - \sum_{1 \leq i_1 < i_2 \leq N_v} \sum_{\mu_1, \mu_2} J_{i_1 i_2}^{\mu_1 \mu_2} \delta_{\mu_1}^{v_{i_1}} \delta_{\mu_2}^{v_{i_2}} + \dots \quad (6)$$

The goal is to derive explicit expressions for the fields H_i^μ and n -th order couplings $J_{i_1 \dots i_n}^{\mu_1 \dots \mu_n}$ in terms of Θ , providing a physical interpretation of the learned model.

We note that model (6) needs gauge fixing, just as we did with the Potts-Bernoulli Hamiltonian. In this case, the lattice-gas gauge condition is

$$H_i^q = J_{i_1 i_2}^{\mu_1 q} = \dots = J_{i_1 \dots i_{N_v}}^{\mu_1 \dots q} = 0, \quad (7)$$

while that of the zero-sum gauge is

$$\sum_{\mu'} \hat{H}_i^{\mu'} = \sum_{\mu'} J_{i_1 i_2}^{\mu_1 \mu'} = \dots = \sum_{\mu'} \hat{J}_{i_1 \dots i_{N_v}}^{\mu_1 \dots \mu'} = 0, \quad (8)$$

for all i, i_1, \dots, i_{N_v} and μ_1, \dots, μ_{N_v} .

Although a gauge transformation does not alter the Boltzmann distribution of the Potts-like model, other functions of the couplings $J_{i_1, \dots, i_n}^{\mu_1, \dots, \mu_n}$, such as the n -th order couplings Fröbenius norm, $F_{i_1 \dots i_n}^{(n)} \stackrel{\text{def}}{=} \left[\sum_{\mu_1, \dots, \mu_n} (J_{i_1 \dots i_n}^{\mu_1 \dots \mu_n})^2 \right]^{\frac{1}{2}}$, is gauge-dependent. In practice, the zero-sum gauge is widely used in inference applications because it minimizes all $F_{i_1 \dots i_n}^{(n)}$, and with it, the strength of high-order couplings by favoring the contribution of low-order couplings [11]. This is also important for the interpretability of models with all-order interactions because, in such situations, one would want to compute an effective low-order Hamiltonian that approximates best the complete effective Hamiltonian [18].

Effective Couplings of an RBM.— Expanding the marginal Hamiltonian (5) in terms of explicit interaction orders yields an effective generalized Potts model, as detailed in (6). For the precise derivation, see Appendix B. The general expression for n -th order effective coupling obtained in such expansion is

$$J_{i_1 \dots i_n}^{\mu_1 \dots \mu_n} = \sum_{K \subseteq [n]} (-1)^{n-|K|} \left[\sum_a \ln \left(1 + e^{c_a + \sum_{k \in K} W_{i_k a}^{\mu_k}} \right) \right], \quad (9)$$

where we introduced the set $[n] = \{1, 2, \dots, n\}$ and $|A|$ to denote the cardinal (i.e., the number of elements) of a given set A . Expression (9) is a general inference formula that maps the weights of an RBM to the physical couplings of a generalized Potts model. When the number of states is $q = 2$, it simplifies to the expressions previously obtained for the lattice gas mapping [23, 24].

Since the zero-sum gauge is more suitable for model inference applications, we have also transformed the expressions in Eq. (9) to this gauge (for the derivation, see Appendix C):

$$\hat{J}_{i_1 \dots i_n}^{\mu_1 \dots \mu_n} = \sum_{K \subseteq [n]} (-1)^{n-|K|} \left[\frac{1}{q^{N_v}} \sum_{\mu'_1, \dots, \mu'_{N_v}} \sum_a \ln \left(1 + e^{c_a + \sum_{k \in K} W_{i_k a}^{\mu'_k} + \sum_{l \in [N_v] \setminus K} W_{i_l a}^{\mu'_l}} \right) \right]. \quad (10)$$

In the above, we have introduced sub-sub-indexes k, l with $k, l \in [N_v]$ to refer to unspecified sites of the system.

Effective Couplings in Generic Probabilistic Models.— Interestingly, Eqs. (10) and (9) can be generalized to any probabilistic model defined on high-dimension categorical space. Formally, any probability mass function π defined over $\Omega \stackrel{\text{def}}{=} \{1, 2, \dots, q\}^{N_v}$, such that $\pi(\mathbf{v}) > 0 \forall \mathbf{v} \in \Omega$, can be mapped into a multibody generalized Potts model (6), whose n -th order couplings are given by

$$J_{i_1 \dots i_n}^{\mu_1 \dots \mu_n} = \sum_{K \subseteq [n]} (-1)^{n-|K|} \mathbb{E}_{\mathbf{u} \sim G} [\ln \pi(\mathbf{u}) | u_{i_k} = \mu_k : k \in K], \quad (11)$$

where, $\mathbb{E}_{\mathbf{u} \sim G} [f(\mathbf{u}) | u_{i_k} = \mu_k : k \in K]$ is the expected value of a function $f : \Omega \rightarrow \mathbb{R}$ with $\mathbf{u} \in \Omega$ following an arbitrary probability measure G but keeping $u_{i_k} = \mu_k$, with $k \in K$. The arbitrariness in G choice reflects the gauge invariance mentioned earlier. For instance, the lattice gas gauge condition (7) is obtained when considering G as the degenerate measure that assigns probability 1 to the configuration (q, q, \dots, q) and 0 to any other $\mathbf{v} \in \Omega$. Moreover, we have the zero-sum gauge if G is uniformly distributed over Ω . It is easy to check that we can recover expressions (9) and (10) by replacing $\pi(\mathbf{v}) \propto \exp \left[\sum_{i,\mu} b_i^\mu \delta_\mu^{v_i} + \sum_a \ln \left(1 + e^{c_a + \sum_{i,\mu} W_{ia}^\mu \delta_\mu^{v_i}} \right) \right]$ in (11) considering G either as the degenerate or the uniform measure, respectively. A general proof of the Potts equivalence and gauge fixing using (11) is provided in App. D. It is worth adding that for energy-based models, i.e., when $\pi(\mathbf{v}) \propto e^{-H(\mathbf{v})}$, we can replace $\ln \pi(\mathbf{v})$ in (11) by the negative energy function $-H(\mathbf{v})$ because the partition function cancels out in the sum.

Large- N approximations.— In general, computing the effective couplings of any order in the zero-sum gauge involves averaging q^{N_v} elements, which is computationally prohibitive in most real-world applications. Previous approaches have extracted pairwise interactions from energy-based models by approximating this average with samples [18, 29], a computationally too demanding

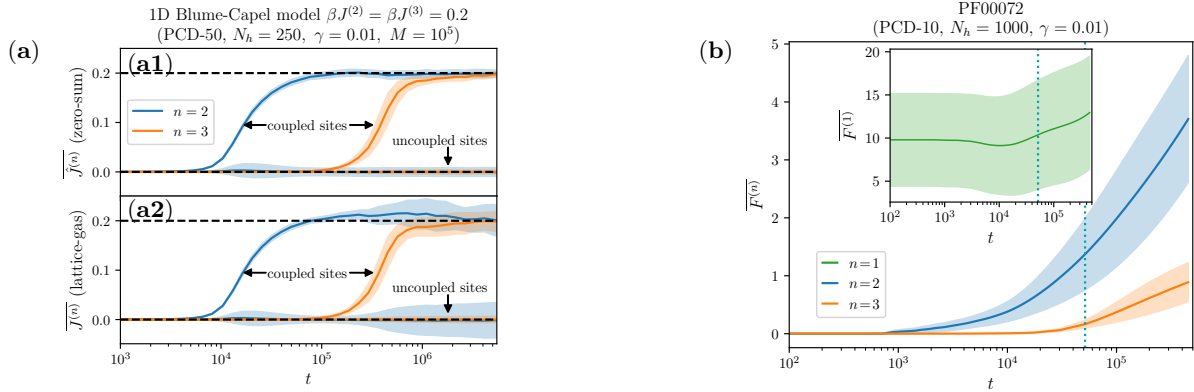


FIG. 2. **Learning dynamics of the effective multibody Potts model.** In (a), we analyze an RBM trained with samples from a spin-1 Blume-Capel model with three-body interactions as defined in Eq. (13), with $\beta J^{(2)} = \beta J^{(3)} = 0.2$. We present the evolution of the averaged effective couplings extracted from the RBM at different training times t . Specifically, we compare the mean values of the inferred couplings, depicted in solid lines (with the standard deviations shown as shaded areas), averaged separately for the coupled and uncoupled terms in the model used to generate the data, against the true values shown in horizontal dashed lines. In (a1), we display the results using the zero-sum gauge, and in (a2), those using the lattice gas gauge. In (b), we analyze an RBM trained with the MSA of the PF00072 protein family. We show the Frobenius norm of the inferred effective model parameters ($n = 1$ for the fields, $n = 2$ for the pairwise coupling tensors, and $n = 3$ for the three-body interactions) as a function of the training time t . A vertical line marks the update at which the best contact prediction performance is achieved, i.e., when the area under the PPV curve is maximal (see Fig. 3 (d)). In both figures, the titles indicate the hyperparameters used for training: PCD- k refers to the persistent contrastive divergence training scheme [31] with k Gibbs steps per update, N_h denotes the number of hidden nodes, and γ represents the learning rate.

method to compute higher-order interactions. Ref. [26] introduces an approximation scheme that leverages the structure of the RBM's energy function and the Central Limit Theorem to approximate the terms inside brackets in (10). By employing this approach to compute the n -th order couplings, we initially reduce the sum over all possible configurations, which contains q^{N_v} elements, to a sum over q^n elements by considering that

$$\begin{aligned} & \frac{1}{q^{N_v}} \sum_{\mu'_1, \dots, \mu'_{N_v}} \ln \left(1 + e^{c_a + \sum_{k=1}^{N_v} W_{i_k a}^{\mu'_k}} \right) \\ &= \frac{1}{q^n} \sum_{\mu'_1, \dots, \mu'_n} \mathbb{E}_{x \sim X} \left[\ln \left(1 + e^{c_a + \sum_{k=1}^n W_{i_k a}^{\mu'_k} + x} \right) \right], \end{aligned} \quad (12)$$

where, $X \stackrel{\text{def}}{=} \sum_{k=n+1}^{N_v} W_{i_k a}^*$, such that $W_{i_k a}^*$ is a random variable uniformly distributed over $\{W_{i_k a}^\mu : \mu \in [q]\}$. Then, by using the central limit theorem and the zero-sum parameters of the RBM, we approximate the right-hand side (r.h.s.) of (12) through the following integral

$$\frac{1}{\sqrt{2\pi}\sigma} \int_{-\infty}^{\infty} dx e^{-\frac{x^2}{2\sigma^2}} \ln \left(1 + e^{c_a + \sum_{k=1}^n W_{i_k a}^\mu + x} \right),$$

with $\sigma = \left[q^{-1} \sum_{k=n+1}^{N_v} \sum_{\mu=1}^q W_{i_k a}^\mu \right]^{\frac{1}{2}}$. The integral mentioned can be approximated using numerical methods, and in our tests, an even discretization of approximately 20 steps has been sufficient to obtain reliable estimates. Furthermore, the calculation of these couplings is straightforward to parallelize, enhancing computation speed. Specifically, the code available on GitHub supports the parallel computation on GPUs of all q^n color

combinations for each n -tuple of interaction sites and fix the zero-sum gauge. Table I in the Appendix details the extraction times for couplings.

Inverse Numerical Experiments – We evaluate the reliability of our approach through an inverse experiment using data generated from a predefined spin-1 Blume-Capel model with 2-body and 3-body interactions. The ground-truth Hamiltonian is:

$$\mathcal{H}_{\mathcal{D}}(\mathbf{s}) = -J^{(3)} \sum_{\langle i,j,k \rangle} s_i s_j s_k - J^{(2)} \sum_{\langle i,j \rangle} s_i s_j, \quad (13)$$

where $s_i \in \{-1, 0, 1\}$. The dataset is generated by sampling $M = 10^5$ equilibrium configurations from the Boltzmann distribution of model (13) at an inverse temperature of $\beta = 0.2$. In particular, we considered a 1D chain of $N = 51$ spins with periodic boundary conditions ($s_{N+1} \equiv s_1$), setting pairwise nearest-neighbor interactions with $J^{(2)} = 1$ and adding sparse three-spin interactions at distant sites with $J^{(3)} = 1$. Specifically, triads involve sites i, j, k satisfying $i \stackrel{\text{def}}{=} j \stackrel{\text{def}}{=} k \pmod{17}$. This 3-state Potts model is particularly appealing as it satisfies both the zero-sum Eq. (8) and lattice gas Eq. (7) gauges simultaneously. This allows for a straightforward comparison of the reliability of the previously introduced lattice-gas and zero-sum effective-coupling formulas.

We train a binary-Potts RBM and extract two- and three-body effective couplings using Eqs. (9) (for the lattice-gas gauge) and (10) (for the zero-sum gauge). We then compare the inferred values with the true ones, separately analyzing coupling and non-coupling links ($J = 0$) in the original model. Fig. 2 (a) shows that RBMs se-

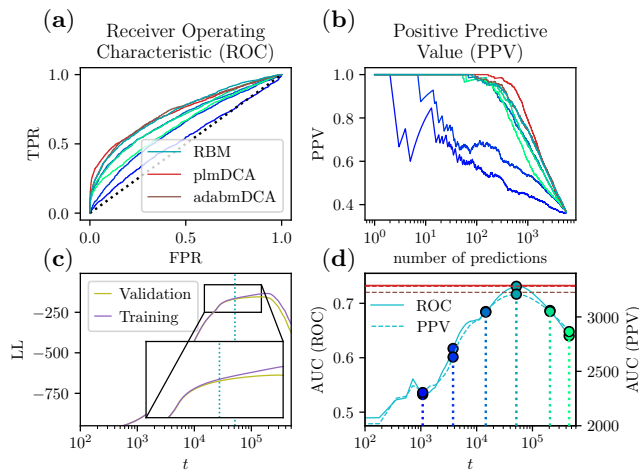


FIG. 3. Contact Prediction with RBMs. We analyze the contact prediction performance of RBMs trained on the MSA for the PF00072 homologous protein family, comparing their accuracy in identifying contacts in the three-dimensional structure against other methods. Panels (a) and (b) display the receiver operating characteristic (ROC) curve and the positive predictive value (PPV) curve as a function of the number of predictions, respectively, with different colors representing various training stages. Panel (c) shows the training and validation log-likelihood (LL) throughout training. In (d), we plot the area under the ROC and PPV curves versus the training time t , with colored dots and lines corresponding to the different training stages shown in (a) and (b). The models presented here were trained using the PCD-10 training scheme, $N_h = 10^3$ hidden nodes, a batch size of 5000, and a learning rate of $\gamma = 0.01$.

quentially learn interactions from lower to higher orders, independent of the gauge used for inference. This aligns with findings in binary RBMs [26] and transformers on language data [32]. We also note that the zero-sum gauge inference (in (a1)) yields more precise values, confirming its superiority for inference.

rbmDCA.— One of the most prominent applications of the inverse Potts problem is predicting contact sites in protein tertiary structures from MSA data [11]. To explore this, we trained a Potts RBM on the MSA of the *response regulator domain* homologous protein family (Pfam entry: PF00072) using the alignment provided in Ref. [33]. For a schematic overview of the analysis pipeline, see Fig. 5 in the Appendix. We then applied our zero-sum mapping (10) (specifically, the pairwise couplings) to compute contact map predictions throughout training (Fig. 2-(b)). These maps were compared against a known 3D structure of the domain and evaluated against established DCA methods, including plmDCA [34, 35], based on pseudo-likelihood maximization and adabmDCA [36, 37], based on Boltzmann machine learning (Fig. 3). In all the analyses conducted in this article, we consider non-trivial contacts, i.e., those residues pair such that $|i - j| > 5$ and physical distance $r < 7.5\text{\AA}$. A detailed description of the *Direct Coupling*

Analysis (DCA) are in Appendix F.

To assess RBM learning quality on this dataset, we computed the log-likelihood (LL) during training using a split dataset (60% training, 40% test), as shown in Fig. 3-(c). The LL was estimated using the *Trajectory Annealing Importance Sampling* method recently introduced in [38]. In Figure 3-(d), we observe that the performance of the RBM training increments with the training time t until it reaches a maximum, where its inference is comparable with other state-of-the-art methods. In particular, we note a similar performance with the adabmDCA, while plmDCA overperforms both. Beyond this point, the prediction performance of the RBM decreases with t due to overfitting but also due to a sharp increase of the MCMC mixing times. Fig. 3-(c) shows that near before the maximum, the log-likelihood w.r.t. the validation set lags behind the increments of the log-likelihood w.r.t. the training. Another indication for overfitting is in Fig. 2-(b), where we see that coupling parameters at all orders do not stabilize but keep growing with t even after the best inference point is reached. We also note that this decline in performance coincides with the emergence of three-body effective couplings (see Fig. 2 (b)) and a sharp drop in both log-likelihoods (LLs). This is primarily driven by a significant increase in the model’s mixing time, which introduces a deterioration in model quality due to non-equilibrium effects [39, 40]. All of the above suggests that, after achieving a good representation of the data, the model begins to overfit low-frequency patterns and co-occurrences, leading to large fields and couplings that make the model relaxation extremely slow. A potential solution could be the implementation of a regularization or pseudo-count strategy during RBM training or using optimized MCMC algorithms for the training, which we leave for future work.

Conclusions.— This paper presented a general framework for interpreting generative models defined on high-dimensional categorical data through a Potts model with many-body interactions. We developed and implemented a protocol that exploits the RBM’s energy structure to extract multi-body couplings from observed data within this framework. We first validated our approach through a controlled experiment, successfully recovering multi-body couplings from synthetic data generated by a modified Blume-Capel model with two-body and three-body interactions. This experiment confirmed that coupling learning is sequential, i.e., an $(n + 1)$ -body interaction is learned only after the n -body interactions are captured—a feature recently observed in deep transformers [32]. Next, we tested the robustness of our approach on the MSA of a protein family. We found that the effective pairwise models extracted from RBM learning could reconstruct the contact map of the protein’s tertiary structure, achieving performance comparable to state-of-the-art methods. Despite these promising results, we also identified overfitting effects that not only lead to the encoding of dataset-specific couplings but also result in the formation of extremely slow relaxation models. This sig-

nificantly hampers training quality as persistent chains fail to converge to equilibrium. Addressing these challenges will be the focus of future work.

Acknowledgments.— The authors acknowledge financial support by the Comunidad de Madrid and the Complutense University of Madrid through the Atracción de Talento program (Refs. 2019-T1/TIC-13298 and Refs. 2023-5A/TIC-28934), and to project PID2021-

125506NA-I00 financed by the "Ministerio de Economía y Competitividad, Agencia Estatal de Investigación" (MICIU/AEI /10.13039/501100011033), and the Fondo Europeo de Desarrollo Regional (FEDER, UE).

Code availability — The code used for training the RBMs is freely available at GitHub:DsysDML/rbms, and the code to extract the couplings is available at GitHub:DsysDML/couplings.inference.

-
- [1] H. C. Nguyen, R. Zecchina, and J. Berg, *Advances in Physics* **66**, 197 (2017).
- [2] E. Schneidman, M. J. Berry, R. Segev, and W. Bialek, *Nature* **440**, 1007 (2006).
- [3] Y. Roudi, E. Aurell, and J. A. Hertz, *Frontiers in computational neuroscience* **3**, 652 (2009).
- [4] L. Meshulam, J. L. Gauthier, C. D. Brody, D. W. Tank, and W. Bialek, *Neuron* **96**, 1178 (2017).
- [5] O. Maoz, G. Tkačik, M. S. Esteki, R. Kiani, and E. Schneidman, *Proceedings of the National Academy of Sciences* **117**, 25066 (2020).
- [6] A. De Martino and D. De Martino, *Heliyon* **4** (2018).
- [7] T. R. Lezon, J. R. Banavar, M. Cieplak, A. Maritan, and N. V. Fedoroff, *Proceedings of the National Academy of Sciences* **103**, 19033 (2006).
- [8] G. Tkačik, C. G. Callan Jr, and W. Bialek, *Proceedings of the National Academy of Sciences* **105**, 12265 (2008).
- [9] F. Morcos, A. Pagnani, B. Lunt, A. Bertolino, D. S. Marks, C. Sander, R. Zecchina, J. N. Onuchic, T. Hwa, and M. Weigt, *Proceedings of the National Academy of Sciences* **108**, E1293 (2011).
- [10] M. Weigt, R. A. White, H. Szurmant, J. A. Hoch, and T. Hwa, *Proceedings of the National Academy of Sciences* **106**, 67 (2009).
- [11] S. Cocco, C. Feinauer, M. Figliuzzi, R. Monasson, and M. Weigt, *Reports on Progress in Physics* **81**, 032601 (2018).
- [12] J. Harte, *Maximum entropy and ecology: a theory of abundance, distribution, and energetics* (OUP Oxford, 2011).
- [13] F. Battiston, E. Amico, A. Barrat, G. Bianconi, G. Ferraz de Arruda, B. Franceschiello, I. Iacopini, S. Kéfi, V. Latora, Y. Moreno, *et al.*, *Nature Physics* **17**, 1093 (2021).
- [14] Y. Roudi, S. Nirenberg, and P. E. Latham, *PLoS computational biology* **5**, e1000380 (2009).
- [15] J. Jumper, R. Evans, A. Pritzel, T. Green, M. Figurnov, O. Ronneberger, K. Tunyasuvunakool, R. Bates, A. Žídek, A. Potapenko, *et al.*, *nature* **596**, 583 (2021).
- [16] J. Abramson, J. Adler, J. Dunger, R. Evans, T. Green, A. Pritzel, O. Ronneberger, L. Willmore, A. J. Ballard, J. Bambrick, *et al.*, *Nature* , 1 (2024).
- [17] R. Rao, J. Meier, T. Sercu, S. Ovchinnikov, and A. Rives, *Biorxiv* , 2020 (2020).
- [18] C. Feinauer, B. Meynard-Piganeau, and C. Lucibello, *PLoS Computational Biology* **18**, e1010219 (2022).
- [19] C. Feinauer and E. Borgonovo, *bioRxiv* , 2022 (2022).
- [20] F. Caredda and A. Pagnani, *bioRxiv* , 2024 (2024).
- [21] P. Smolensky, In parallel distributed processing: Volume 1 by d. rumelhart and j. mclelland (MIT Press, 1986) Chap. 6: Information Processing in Dynamical Systems: Foundations of Harmony Theory.
- [22] N. Le Roux and Y. Bengio, *Neural computation* **20**, 1631 (2008).
- [23] G. Cossu, L. Del Debbio, T. Giani, A. Khamseh, and M. Wilson, *Physical Review B* **100**, 064304 (2019).
- [24] N. Bulso and Y. Roudi, *Neural Computation* **33**, 2646 (2021).
- [25] S. Feng, D. Kong, and N. Trivedi, *arXiv preprint arXiv:2302.03212* (2023).
- [26] A. Decelle, C. Furtlehner, A. d. J. Navas Gómez, and B. Seoane, *SciPost Physics* **16**, 095 (2024).
- [27] G. di Sarra, B. Bravi, and Y. Roudi, *Europhysics Letters* (2025).
- [28] S. Cocco, A. De Martino, A. Pagnani, M. Weigt, and F. Ritort, in *Spin Glass Theory and Far Beyond: Replica Symmetry Breaking After 40 Years* (World Scientific, 2023).
- [29] J. Tubiana, S. Cocco, and R. Monasson, *Elife* **8**, e39397 (2019).
- [30] A. Decelle, B. Seoane, and L. Rosset, *Physical Review E* **108**, 014110 (2023).
- [31] T. Tieleman, in *Proceedings of the 25th international conference on Machine learning* (2008) pp. 1064–1071.
- [32] R. Rende, F. Gerace, A. Laio, and S. Goldt, *arXiv preprint arXiv:2410.19637* (2024).
- [33] J. Trinquier, G. Uguzzoni, A. Pagnani, F. Zamponi, and M. Weigt, *Nature communications* **12**, 5800 (2021).
- [34] M. Ekeberg, C. Lövkvist, Y. Lan, M. Weigt, and E. Aurell, *Physical Review E—Statistical, Nonlinear, and Soft Matter Physics* **87**, 012707 (2013).
- [35] M. Ekeberg, T. Hartonen, and E. Aurell, *Journal of Computational Physics* **276**, 341 (2014).
- [36] A. P. Muntoni, A. Pagnani, M. Weigt, and F. Zamponi, *BMC bioinformatics* **22**, 1 (2021).
- [37] L. Rosset, R. Netti, A. P. Muntoni, M. Weigt, and F. Zamponi, *arXiv preprint arXiv:2501.18456* (2025).
- [38] N. Béreux, A. Decelle, C. Furtlehner, L. Rosset, and B. Seoane, *International Conference on Learning Representations* (2025), *arXiv:2405.15376* (2025).
- [39] A. Decelle, C. Furtlehner, and B. Seoane, *Advances in Neural Information Processing Systems* **34**, 5345 (2021).
- [40] E. Agoritsas, G. Catania, A. Decelle, and B. Seoane, in *ICML 2023-40th International Conference on Machine Learning* (2023).
- [41] M. Blume, *Physical Review* **141**, 517 (1966).
- [42] H. Capel, *Physica* **32**, 966 (1966).
- [43] R. Durbin, S. R. Eddy, A. Krogh, and G. Mitchison, *Biological sequence analysis: probabilistic models of proteins and nucleic acids* (Cambridge University Press, 1998).
- [44] S. D. Dunn, L. M. Wahl, and G. B. Gloor, *Bioinformatics* **24**, 333 (2008).

- [45] L. Burger and E. Van Nimwegen, PLoS computational biology **6**, e1000633 (2010).
- [46] C. Feinauer, *The Statistical Mechanics Approach to Protein Sequence Data: Beyond Contact Prediction*, Ph.D. thesis, Politecnico di Torino, Turin, Italy (2016).
- [47] J. Fernandez-de Cossio-Diaz, in *RNA Design: Methods and Protocols* (Springer, 2024) pp. 163–175.
- [48] C. W. Lynn, Q. Yu, R. Pang, S. E. Palmer, and W. Bialek, arXiv preprint arXiv:2402.00007 (2023).
- [49] D. H. Ackley, G. E. Hinton, and T. J. Sejnowski, Cognitive science **9**, 147 (1985).
- [50] M. Figliuzzi, P. Barrat-Charlaix, and M. Weigt, Molecular biology and evolution **35**, 1018 (2018).
- [51] S. Zamuner and P. D. L. Rios, arXiv preprint arXiv:2102.03202 (2021).
- [52] A. Decelle, A. d. J. Navas Gómez, and B. Seoane, Supplementary Material (2025).

Appendix A: Training of the RBM

Our RBMs are trained by maximizing the log-likelihood function $\mathcal{L}(\Theta|\mathcal{D})$, which quantifies the probability of observing a given dataset $\mathcal{D} = \{\mathbf{v}^{(1)}, \dots, \mathbf{v}^{(M)}\}$ under a probabilistic model parameterized by Θ . The optimization objective is then formally expressed as:

$$\mathcal{L}(\mathcal{D}|\Theta) = \frac{1}{M} \sum_{m=1}^M \log p_{\Theta}(\mathbf{v}^{(m)}) = \frac{1}{M} \sum_{m=1}^M \log \sum_{\mathbf{h}} e^{-\mathcal{H}_{\Theta}(\mathbf{v}^{(m)}, \mathbf{h})} - \log Z_{\Theta}. \quad (\text{A1})$$

We optimize $\mathcal{L}(\Theta|\mathcal{D})$ using the (stochastic) gradient descent algorithm. For our RBM, the gradient is given by:

$$\begin{aligned} \frac{\partial \mathcal{L}}{\partial b_i^{\mu}} &= \langle \delta_{\mu}^{v_i} \rangle_{\mathcal{D}} - \langle \delta_{\mu}^{v_i} \rangle_{\mathcal{H}}, & \frac{\partial \mathcal{L}}{\partial c_a} &= \langle h_a \rangle_{\mathcal{D}} - \langle h_a \rangle_{\mathcal{H}}, \\ \text{and } \frac{\partial \mathcal{L}}{\partial W_{ia}^{\mu}} &= \langle h_a \delta_{\mu}^{v_i} \rangle_{\mathcal{D}} - \langle h_a \delta_{\mu}^{v_i} \rangle_{\mathcal{H}}, \end{aligned} \quad (\text{A2})$$

where $\langle f(\mathbf{v}, \mathbf{h}) \rangle_{\mathcal{D}} = M^{-1} \sum_m \sum_{\{\mathbf{h}\}} f(\mathbf{v}^{(m)}, \mathbf{h}) p(\mathbf{h}|\mathbf{v}^{(m)})$ represents the expectation of $f(\mathbf{v}, \mathbf{h})$ over the dataset, and $\langle f(\mathbf{v}, \mathbf{h}) \rangle_{\mathcal{H}}$ denotes the expectation with respect to the Boltzmann distribution of the model, whose Hamiltonian is defined in (2).

Since computing the partition function is typically intractable, the second average is approximated using Markov Chain Monte Carlo (MCMC) and the Alternating Gibbs Sampling algorithm. This algorithm exploits the bipartite structure of the RBM, iteratively sampling the visible and hidden variables conditioned on the other layer. This approach enables efficient parallelization, significantly accelerating the sampling process.

In this work, we trained RBMs using the persistent contrastive divergence (PCD- k) algorithm [31], where the Markov chains for gradient estimation are initialized from the final states of the previous update and evolved for k Gibbs steps. This approach has been shown to yield quasi-equilibrium models [39]. We further verified that the learned models operated in the equilibrium regime [39, 40], exhibiting no memory of the training scheme when sampled for generation.

Appendix B: Deriving the Effective lattice gas Model

In Ref. [23], a Bernoulli-Bernoulli RBM (i.e., $v_i, h_a \in \{0, 1\}$) was mapped onto a multi-body Ising-like model of binary variables. The following section extends this approach to derive a mapping for an arbitrary number of colors q . Marginalizing the Boltzmann distribution (1) yields:

$$p(\mathbf{v}) = \frac{1}{\mathcal{Z}} \sum_{\mathbf{h}} e^{-\mathcal{H}(\mathbf{v}, \mathbf{h})} = \frac{1}{\mathcal{Z}} e^{-H(\mathbf{v})}. \quad (\text{B1})$$

By substituting the RBM Hamiltonian from Eq. (2) into this expression, and summing over the hidden nodes, we obtain:

$$H(\mathbf{v}) = - \sum_{i, \mu} b_i^{\mu} \delta_{\mu}^{v_i} - \sum_a \ln \sum_{h_a} e^{c_a h_a + h_a \sum_{i, \mu} W_{ia}^{\mu} \delta_{\mu}^{v_i}}. \quad (\text{B2})$$

Now we define

$$q(h_a) \stackrel{\text{def}}{=} e^{c_a h_a} \text{ and } t \stackrel{\text{def}}{=} \sum_{i,\mu} W_{ia}^\mu \delta_\mu^{v_i}, \quad (\text{B3})$$

to introduce the following *cumulant*-generating function

$$K_a(t) \stackrel{\text{def}}{=} \ln \sum_{h_a} q(h_a) e^{h_a t} = \sum_{k=0}^{\infty} \frac{\kappa_a^{(k)} t^k}{k!} \quad (\text{B4a})$$

$$= \ln(1 + e^{c_a + t}), \quad (\text{B4b})$$

where the k -th cumulant is

$$\kappa_a^{(k)} = \left. \frac{\partial^k K_a(t)}{\partial t^k} \right|_{t=0}. \quad (\text{B5})$$

Replacing Eq. (B4a) into Eq. (B2) yields:

$$H(\mathbf{v}) = - \sum_{i,\mu} b_i^\mu \delta_\mu^{v_i} - \sum_{a,k} \frac{\kappa_a^{(k)} t^k}{k!}.$$

Considering the definition (B3), we can rewrite the above expression as

$$H(\mathbf{v}) = - \sum_a \kappa_a^{(0)} - \sum_{i,a} \left(b_i^\mu + \sum_a \kappa_a^{(1)} W_{ia}^\mu \right) \delta_\mu^{v_i} - \sum_{k>1} \frac{1}{k!} \sum_{i_1, \dots, i_k} \sum_{\mu_1, \dots, \mu_k} \left(\sum_a \kappa_a^{(k)} W_{i_1 a}^{\mu_1} \dots W_{i_k a}^{\mu_k} \right) \delta_{\mu_1}^{v_{i_1}} \dots \delta_{\mu_k}^{v_{i_k}}. \quad (\text{B6})$$

Here, we note that high-order terms in k also contribute to the n -body coupling constants, where n is the number of distinct sites. Since

$$\delta_{\mu_1}^{v_{i_1}} \delta_{\mu_2}^{v_{i_2}} \dots \delta_{\mu_k}^{v_{i_k}} = \begin{cases} \delta_\mu^{v_i} & \text{if } \mu = \mu_1 = \mu_2 = \dots = \mu_k, \\ 0 & \text{otherwise,} \end{cases}$$

high-order terms cancel out if they include factors of visible variables with different colors on the same site. Then, for each k in (B6), the sum over the visible sites i_1, \dots, i_k can be grouped by the number n of distinct sites being considered. Thus, the term of (B6) that includes solely sites i_1 and i_2 , considering the contributions of all orders in k , is given by

$$\begin{aligned} & \sum_{k>1} \frac{1}{k!} \sum_{l=1}^{k-1} \sum_{1 \leq i_1 < i_2 \leq N_v} \sum_{\mu_1, \mu_2} \left(\sum_a \kappa_a^{(k)} \binom{k}{l} (W_{i_1 a}^{\mu_1})^l (W_{i_2 a}^{\mu_2})^{k-l} \right) \delta_{\mu_1}^{v_{i_1}} \delta_{\mu_2}^{v_{i_2}} \\ &= \sum_{k>1} \frac{1}{k!} \sum_{1 \leq i_1 < i_2 \leq N_v} \sum_{\mu_1, \mu_2} \left(\sum_a \kappa_a^{(k)} \left[(W_{i_1 a}^{\mu_1} + W_{i_2 a}^{\mu_2})^k - (W_{i_1 a}^{\mu_1})^k - (W_{i_2 a}^{\mu_2})^k \right] \right) \delta_{\mu_1}^{v_{i_1}} \delta_{\mu_2}^{v_{i_2}}. \end{aligned}$$

The direct comparison of the above with (6) implies that

$$J_{i_1 i_2}^{\mu_1 \mu_2} = \sum_{k>1} \frac{1}{k!} \sum_a \kappa_a^{(k)} \left[(W_{i_1 a}^{\mu_1} + W_{i_2 a}^{\mu_2})^k - (W_{i_1 a}^{\mu_1})^k - (W_{i_2 a}^{\mu_2})^k \right]. \quad (\text{B7})$$

Replacing (B5) in (B7) gives

$$\begin{aligned} J_{i_1 i_2}^{\mu_1 \mu_2} &= \sum_{k>1} \frac{1}{k!} \sum_a \left[(W_{i_1 a}^{\mu_1} + W_{i_2 a}^{\mu_2})^k - (W_{i_1 a}^{\mu_1})^k - (W_{i_2 a}^{\mu_2})^k \right] \left. \frac{\partial^k K_a(t)}{\partial t^k} \right|_{t=0} \\ &= \sum_a \sum_k \frac{1}{k!} \left[(W_{i_1 a}^{\mu_1} + W_{i_2 a}^{\mu_2})^k - (W_{i_1 a}^{\mu_1})^k - (W_{i_2 a}^{\mu_2})^k \right] \left. \frac{\partial^k K_a(t)}{\partial t^k} \right|_{t=0} + \sum_a K_a(0) \\ &= \sum_i \left[e^{(W_{i_1 a}^{\mu_1} + W_{i_2 a}^{\mu_2}) \partial_t} - e^{W_{i_1 a}^{\mu_1} \partial_t} - e^{W_{i_2 a}^{\mu_2} \partial_t} + 1 \right] K_i(t) \Big|_{t=0}. \end{aligned}$$

In the above expression, we identify the shift (or translation) operator

$$e^{a\partial_x} f(x) \stackrel{\text{def}}{=} f(a+x), \quad (\text{B8})$$

which gives us

$$J_{i_1 i_2}^{\mu_1 \mu_2} = \sum_a [K_a (W_{i_1 a}^{\mu_1} + W_{i_2 a}^{\mu_2}) - K_a (W_{i_1 a}^{\mu_1}) - K_a (W_{i_2 a}^{\mu_2}) + K_a(0)]. \quad (\text{B9})$$

Using definition (B4b) in (B9) leads automatically to

$$J_{i_1 i_2}^{\mu_1 \mu_2} = \sum_a \ln \frac{(1 + e^{c_a + W_{i_1 a}^{\mu_1} + W_{i_2 a}^{\mu_2}})(1 + e^{c_a})}{(1 + e^{c_a + W_{i_1 a}^{\mu_1}})(1 + e^{c_a + W_{i_2 a}^{\mu_2}})}. \quad (\text{B10})$$

Similarly, the field contributions in (B6) can be written as

$$- \sum_{i, \mu} \left(b_i^\mu + \sum_a \kappa_a^{(1)} W_{i_1 a}^\mu \right) \delta_\mu^{v_i} - \sum_{k>1} \frac{1}{k!} \sum_{i, \mu} \left(\sum_a \kappa_a^{(k)} (W_{i_1 a}^\mu)^k \right) \delta_\mu^{v_i}. \quad (\text{B11})$$

Developing the left-side term in the above:

$$\begin{aligned} \sum_{k>1} \frac{1}{k!} \sum_a \kappa_a^{(k)} (W_{i_1 a}^\mu)^k &= \sum_{k \geq 0} \frac{1}{k!} \sum_a (W_{i_1 a}^\mu)^k \left. \frac{\partial^k K_a(t)}{\partial t^k} \right|_{t=0} - \sum_a K_a(0) - \sum_a \kappa_a^{(1)} W_{i_1 a}^\mu \\ &= \sum_a e^{W_{i_1 a}^\mu \partial_t} K_a(t) \Big|_{t=0} - \sum_a K_a(0) - \sum_a \kappa_a^{(1)} W_{i_1 a}^\mu \\ &= \sum_a \left[K_i(W_{i_1 a}^\mu) - K_a(0) - \kappa_i^{(1)} W_{i_1 a}^\mu \right] \\ &= \sum_a \left[\ln \left(\frac{1 + e^{c_i + W_{i_1 a}^\mu}}{1 + e^{c_i}} \right) - \kappa_i^{(1)} W_{i_1 a}^\mu \right]. \end{aligned} \quad (\text{B12})$$

Finally, substituting (B12) in (B11) and comparing with (6) we obtain that the effective fields are given by

$$H_i^\mu = b_i^\mu + \sum_a \ln \left(\frac{1 + e^{c_a + W_{i_1 a}^\mu}}{1 + e^{c_a}} \right) \stackrel{\text{def}}{=} b_i^\mu + J_i^\mu, \quad (\text{B13})$$

where we denoted by J_i^μ the contribution to the effective fields due to the interaction with the hidden variables. An analogous procedure can be applied by considering the contributions from all k -order terms to any n -th order interaction in Eq. (B6), allowing us to derive the corresponding coupling constant. The general expression was given by Eq. (9) in the main text, which we repeat here for clarity:

$$J_{i_1 \dots i_n}^{\mu_1 \dots \mu_n} = \sum_{K \subseteq [n]} (-1)^{n-|K|} \left[\sum_a \ln \left(1 + e^{c_a + \sum_{k \in K} W_{i_k a}^{\mu_k}} \right) \right].$$

Finally, to verify that the couplings written in this formulation satisfy the lattice gas condition (7), we set the RBM in its corresponding lattice gas gauge (i.e., $b_j^q = W_{ij}^q = 0$ for all i, j) then it is easy to see that

$$\begin{aligned} H_i^q &= b_i^q + \sum_a \ln \left(\frac{1 + e^{c_a + W_{i_1 a}^q}}{1 + e^{c_a}} \right) = 0, \text{ and} \\ J_{i_1 i_2}^{\mu_1 q} &= \sum_a \ln \frac{(1 + e^{c_a + W_{i_1 a}^{\mu_1} + W_{i_2 a}^q})(1 + e^{c_a})}{(1 + e^{c_a + W_{i_1 a}^{\mu_1}})(1 + e^{c_a + W_{i_2 a}^q})} = 0. \end{aligned}$$

Thus, in general, we have

$$J_{i_1 \dots i_n}^{\mu_1 \dots q} = \sum_{K \subseteq [n-1]} \sum_a \left[(-1)^{n-|K|} \ln \left(1 + e^{c_a + \sum_{k \in K} W_{i_k a}^{\mu_k}} \right) - (-1)^{n-|K|} \ln \left(1 + e^{c_a + \sum_{n \in K} W_{i_k a}^{\mu_k} + W_{i_n a}^q} \right) \right] = 0.$$

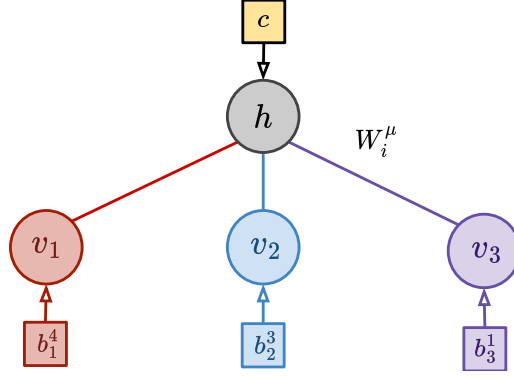


FIG. 4. Diagram of the 3-visible hidden nodes RBM we use to derive the exact mapping in the zero-sum Gauge.

Appendix C: Deriving the Effective Zero-Sum Model

Since directly addressing the gauge transformation of model (6) for a general RBM can be challenging, we begin with a more tractable system: a hidden node connected to only three visible variables (see Fig. 4). In this case, the effective Potts Hamiltonian includes up to three-body interactions:

$$H(\mathbf{v}) = - \sum_{i,\mu} H_i^\mu \delta_\mu^{v_{i1}} - \sum_{i_1 < i_2} \sum_{\mu_1, \mu_2} J_{i_1 i_2}^{\mu_1 \mu_2} \delta_{\mu_1}^{v_{i_1}} \delta_{\mu_2}^{v_{i_2}} - \sum_{i_1 < i_2 < i_3} \sum_{\mu_1, \mu_2, \mu_3} J_{i_1 i_2 i_3}^{\mu_1 \mu_2 \mu_3} \delta_{\mu_1}^{v_{i_1}} \delta_{\mu_2}^{v_{i_2}} \delta_{\mu_3}^{v_{i_3}}. \quad (\text{C1})$$

Without loss of generality, we assume that the above Hamiltonian is written in the lattice gas gauge as derived in Appendix B. We obtain effective pairwise couplings and fields in the zero-sum gauge by applying the following gauge transformations:

$$\begin{aligned} \hat{J}_{i_1 i_2}^{\mu_1 \mu_2} &\stackrel{\text{def}}{=} J_{i_1 i_2}^{\mu_1 \mu_2} - \frac{1}{q} \left(\sum_{\mu'_1} J_{i_1 i_2}^{\mu'_1 \mu_2} + \sum_{\mu'_2} J_{i_1 i_2}^{\mu_1 \mu'_2} \right) + \frac{1}{q^2} \sum_{\mu'_1, \mu'_2} J_{i_1 i_2}^{\mu'_1 \mu'_2} \\ &\quad + \frac{1}{q} \sum_{\mu'_3} J_{i_1 i_2 i_3}^{\mu_1 \mu_2 \mu'_3} - \frac{1}{q^2} \left(\sum_{\mu'_1, \mu'_3} J_{i_1 i_2 i_3}^{\mu'_1 \mu_2 \mu'_3} + \sum_{\mu'_2, \mu'_3} J_{i_1 i_2 i_3}^{\mu_1 \mu'_2 \mu'_3} \right) + \frac{1}{q^3} \sum_{\mu'_1, \mu'_2, \mu'_3} J_{i_1 i_2 i_3}^{\mu'_1 \mu'_2 \mu'_3} \end{aligned} \quad (\text{C2})$$

$$\begin{aligned} \hat{H}_{i_1}^{\mu_1} &\stackrel{\text{def}}{=} H_{i_1}^{\mu_1} - \frac{1}{q} \sum_{\mu'_1} H_{i_1}^{\mu'_1} + \sum_{i_2} \left(\frac{1}{q} \sum_{\mu'_2} J_{i_1 i_2}^{\mu_1 \mu'_2} - \frac{1}{q^2} \sum_{\mu'_1, \mu'_2} J_{i_1 i_2}^{\mu'_1 \mu'_2} \right) \\ &\quad + \frac{1}{q^2} \sum_{\mu'_2, \mu'_3} J_{i_1 i_2 i_3}^{\mu_1 \mu'_2 \mu'_3} - \frac{1}{q^3} \sum_{\mu'_1, \mu'_2, \mu'_3} J_{i_1 i_2 i_3}^{\mu'_1 \mu'_2 \mu'_3}, \end{aligned} \quad (\text{C3})$$

where, we always kept $i_1 \neq i_2, i_3$ and $i_2 \neq i_3$. Using the shift operation, introduced in (B8), we find the following recurrence relation in the general expression for couplings in the lattice gas gauge:

$$J_{i_1 \dots i_n}^{\mu_1 \dots \mu_n} = \left(e^{W_{i_n}^{\mu_n} \partial_c} - 1 \right) \sum_{K \subseteq [N-1]} (-1)^{n-1-|K|} \ln \left(1 + e^{c + \sum_{k \in K} W_{i_k}^{\mu_k}} \right) = \left(e^{W_{i_n}^{\mu_n} \partial_c} - 1 \right) J_{i_1 \dots i_{n-1}}^{\mu_1 \dots \mu_{n-1}}. \quad (\text{C4})$$

Using (C4) to operate in (C2) gives

$$\begin{aligned}
\hat{j}_{i_1 i_2}^{\mu_1 \mu_2} &= J_{i_1 i_2}^{\mu_1 \mu_2} - \frac{1}{q} \left(\sum_{\mu'_1} J_{i_1 i_2}^{\mu'_1 \mu_2} + \sum_{\mu'_2} J_{i_1 i_2}^{\mu_1 \mu'_2} \right) + \frac{1}{q^2} \sum_{\mu'_1, \mu'_2} J_{i_1 i_2}^{\mu'_1 \mu'_2} \\
&+ \frac{1}{q} \sum_{\mu'_3} \left(e^{W_{i_3}^{\mu'_3} \partial_c} - 1 \right) \left(J_{i_1 i_2}^{\mu_1 \mu_2} - \frac{1}{q} \left(\sum_{\mu'_1} J_{i_1 i_2}^{\mu'_1 \mu_2} + \sum_{\mu'_2} J_{i_1 i_2}^{\mu_1 \mu'_2} \right) + \frac{1}{q^2} \sum_{\mu'_1, \mu'_2} J_{i_1 i_2}^{\mu'_1 \mu'_2} \right) \\
&= \frac{1}{q} \sum_{\mu'_3} e^{W_{i_3}^{\mu'_3} \partial_c} \left(J_{i_1 i_2}^{\mu_1 \mu_2} - \frac{1}{q} \left(\sum_{\mu'_1} J_{i_1 i_2}^{\mu'_1 \mu_2} + \sum_{\mu'_2} J_{i_1 i_2}^{\mu_1 \mu'_2} \right) + \frac{1}{q^2} \sum_{\mu'_1, \mu'_2} J_{i_1 i_2}^{\mu'_1 \mu'_2} \right) \\
&= \frac{1}{q^3} \sum_{\mu'_1, \mu'_2, \mu'_3} e^{W_{i_3}^{\mu'_3} \partial_c} \left(J_{i_1 i_2}^{\mu_1 \mu_2} - J_{i_1 i_2}^{\mu'_1 \mu_2} - J_{i_1 i_2}^{\mu_1 \mu'_2} + J_{i_1 i_2}^{\mu'_1 \mu'_2} \right). \tag{C5}
\end{aligned}$$

Then, we obtain the expression for the pairwise couplings in the zero-sum gauge by replacing (B10) in the above

$$\hat{j}_{i_1 i_2}^{\mu_1 \mu_2} = \frac{1}{q^3} \sum_{\mu'_1, \mu'_2, \mu'_3} \ln \frac{\left(1 + e^{c+W_{i_1}^{\mu'_1}+W_{i_2}^{\mu'_2}+W_{i_3}^{\mu'_3}} \right) \left(1 + e^{c+W_{i_1}^{\mu'_1}+W_{i_2}^{\mu'_2}+W_{i_3}^{\mu'_3}} \right)}{\left(1 + e^{c+W_{i_1}^{\mu'_1}+W_{i_2}^{\mu'_2}+W_{i_3}^{\mu'_3}} \right) \left(1 + e^{c+W_{i_1}^{\mu'_1}+W_{i_2}^{\mu'_2}+W_{i_3}^{\mu'_3}} \right)}. \tag{C6}$$

Similarly, for the fields, we can write

$$\begin{aligned}
\hat{H}_{i_1}^{\mu_1} &= b_{i_1}^{\mu_1} - \frac{1}{q} \sum_{\mu'_1} b_{i_1}^{\mu'_1} + J_{i_1}^{\mu_1} - \frac{1}{q} \sum_{\mu'_1} J_{i_1}^{\mu'_1} \\
&- \frac{1}{q} \sum_{\mu'_3} \left(e^{W_{i_3}^{\mu'_3} \partial_c} - 1 \right) \left(J_{i_1}^{\mu_1} - \frac{1}{q} \sum_{\mu'_1} J_{i_1}^{\mu'_1} \right) - \frac{1}{q} \sum_{\mu'_2} \left(e^{W_{i_2}^{\mu'_2} \partial_c} - 1 \right) \left(J_{i_1}^{\mu_1} - \frac{1}{q} \sum_{\mu'_1} J_{i_1}^{\mu'_1} \right) \\
&+ \frac{1}{q^2} \sum_{\mu'_2, \mu'_3} \left(e^{W_{i_2}^{\mu'_2} \partial_c} - 1 \right) \left(e^{W_{i_3}^{\mu'_3} \partial_c} - 1 \right) \left(J_{i_1}^{\mu_1} - \frac{1}{q} \sum_{\mu'_1} J_{i_1}^{\mu'_1} \right) \\
&= b_{i_1}^{\mu_1} - \frac{1}{q} \sum_{\mu'_1} b_{i_1}^{\mu'_1} + \frac{1}{q^3} \sum_{\mu_1, \mu'_2, \mu'_3} e^{(W_{i_2}^{\mu'_2} + W_{i_3}^{\mu'_3}) \partial_c} \left(J_{i_1}^{\mu_1} - J_{i_1}^{\mu'_1} \right). \tag{C7}
\end{aligned}$$

Replacing the lattice gas coupling definition given in (B13) in the above gives

$$\hat{H}_{i_1}^{\mu_1} = \hat{b}_{i_1}^{\mu_1} + \frac{1}{q^3} \sum_{\mu'_1, \mu'_2, \mu'_3} \ln \left(\frac{1 + e^{c_a + W_{i_1}^{\mu_1} + W_{i_2}^{\mu'_2} + W_{i_3}^{\mu'_3}}}{1 + e^{c_a + W_{i_1}^{\mu'_1} + W_{i_2}^{\mu'_2} + W_{i_3}^{\mu'_3}}} \right), \tag{C8}$$

where we denote by $\hat{b}_{i_1}^{\mu_1}$ the visible biases in the zero-sum gauge. Following this kind of construction, we can write the expression for effective pairwise and fields for an RBM with an arbitrary number of hidden and visible nodes:

$$\hat{j}_{i_1 i_2}^{\mu_1 \mu_2} = \frac{1}{q^{N_V}} \sum_{\mu'_1, \dots, \mu'_{N_V}} \sum_a \ln \frac{\left(1 + e^{c + W_{i_1 a}^{\mu_1} + W_{i_2 a}^{\mu_2} + \sum_{k=3}^{N_V} W_{i_k a}^{\mu'_k}} \right) \left(1 + e^{c + W_{i_1 a}^{\mu'_1} + W_{i_2 a}^{\mu'_2} + \sum_{k=3}^{N_V} W_{i_k a}^{\mu'_k}} \right)}{\left(1 + e^{c + W_{i_1 a}^{\mu'_1} + W_{i_2 a}^{\mu'_2} + \sum_{k=3}^{N_V} W_{i_k a}^{\mu'_k}} \right) \left(1 + e^{c + W_{i_1 a}^{\mu'_1} + W_{i_2 a}^{\mu'_2} + \sum_{k=3}^{N_V} W_{i_k a}^{\mu'_k}} \right)}, \tag{C9}$$

$$\hat{H}_{i_1}^{\mu_1} = \hat{b}_{i_1}^{\mu_1} + \frac{1}{q^{N_V}} \sum_{\mu'_1, \dots, \mu'_{N_V}} \sum_a \ln \left(\frac{1 + e^{c_a + W_{i_1 a}^{\mu_1} + W_{i_2 a}^{\mu'_2} + \sum_{k=3}^{N_V} W_{i_k a}^{\mu'_k}}}{1 + e^{c_a + W_{i_1 a}^{\mu'_1} + W_{i_2 a}^{\mu'_2} + \sum_{k=3}^{N_V} W_{i_k a}^{\mu'_k}}} \right). \tag{C10}$$

Moreover, we can further generalize the above by considering an arbitrary n -th order coupling, leading to formula (10) in the main text, which we repeat here for completeness:

$$\hat{j}_{i_1 \dots i_n}^{\mu_1 \dots \mu_n} = \sum_{K \subseteq [n]} (-1)^{n-|K|} \left[\frac{1}{q^{N_V}} \sum_{\mu'_1, \dots, \mu'_{N_V}} \sum_a \ln \left(1 + e^{c_a + \sum_{k \in K} W_{i_k a}^{\mu_k} + \sum_{l \in [N_V] \setminus K} W_{i_l a}^{\mu'_l}} \right) \right].$$

Appendix D: Gauge fixing of the multi-body Potts model

In Refs. [18, 19], Feinauer et al. demonstrated that the Hamiltonians of energy-based models can be expressed as Potts-like Hamiltonians with multi-body interactions in the zero-sum gauge. In [18], they also derived a sampling estimator to compute effective pairwise couplings and fields in such a gauge. Building upon this foundation, we extend our findings from the RBM case to establish a general mapping between probabilistic models and generalized Potts-like models, as defined in Eq. (6), with couplings given by Eq. (11). To validate this approach, we now prove that this Potts-like formulation preserves the probability mass distribution, which is equivalent to proving the following theorem:

Theorem 1. Gauge Invariance. *Let π be a probability mass function defined over the sample space $\Omega \stackrel{\text{def}}{=} \{1, 2, \dots, q\}^N$, such that $\pi(\mathbf{v}) > 0$ for all $\mathbf{v} \in \Omega$. Then, the relation $\pi(\mathbf{v}) \propto e^{-\mathcal{H}(\mathbf{v})}$ holds, given the Hamiltonian definition:*

$$\begin{aligned} \mathcal{H}(\mathbf{v}) &= - \sum_{n=1}^N \sum_{i_1=1}^{N-n+1} \sum_{i_2=i_1+1}^{N-n+2} \dots \sum_{i_n=i_{n-1}+1}^N \sum_{\mu_1=1}^q \dots \sum_{\mu_n=1}^q J_{i_1 \dots i_n}^{\mu_1 \dots \mu_n} \delta_{\mu_1}^{v_{i_1}} \dots \delta_{\mu_n}^{v_{i_n}} \\ &= - \sum_{n=1}^N \sum_{i_1=1}^{N-n+1} \sum_{i_2=i_1+1}^{N-n+2} \dots \sum_{i_n=i_{n-1}+1}^N \sum_{K \subseteq [n]} (-1)^{n-|K|} \mathbb{E}_{\mathbf{u} \sim G} [\ln \pi(\mathbf{u}) | u_{i_k} = v_{i_k} : k \in K]. \end{aligned} \quad (\text{D1})$$

for any probability measure G defined over Ω .

Proof. Here, we will use an *induction* argument in N . Let us choose $N = 2$ as our *base case* for didactical reasons. When $N = 2$, it is then straightforward to obtain that

$$\begin{aligned} \mathcal{H}(\mathbf{v}) &= -J_1^{v_1} - J_2^{v_2} - J_1^{v_1 v_2} \\ &= -(\mathbb{E}_{\mathbf{u} \sim G} [\ln \pi(\mathbf{u}) | u_1 = v_1] - \mathbb{E}_{\mathbf{u} \sim G} [\ln \pi(\mathbf{u})]) - (\mathbb{E}_{\mathbf{u} \sim G} [\ln \pi(\mathbf{u}) | u_2 = v_2] - \mathbb{E}_{\mathbf{u} \sim G} [\ln \pi(\mathbf{u})]) \\ &\quad - (\mathbb{E}_{\mathbf{u} \sim G} [\ln \pi(\mathbf{u}) | u_1 = v_1, u_2 = v_2] - \mathbb{E}_{\mathbf{u} \sim G} [\ln \pi(\mathbf{u}) | u_1 = v_1] - \mathbb{E}_{\mathbf{u} \sim G} [\ln \pi(\mathbf{u}) | u_2 = v_2] + \mathbb{E}_{\mathbf{u} \sim G} [\ln \pi(\mathbf{u})]) \\ &= -\ln \pi(\mathbf{v}) + \mathbb{E}_{\mathbf{u} \sim G} [\ln \pi(\mathbf{u})]. \end{aligned} \quad (\text{D2})$$

In the above we recognized that $\mathbb{E}_{\mathbf{u} \sim G} [\ln \pi(\mathbf{u}) | u_1 = v_1, u_2 = v_2] = \ln \pi(\mathbf{v})$, with $\mathbf{v} = (v_1, v_2)$. Since $\mathbb{E}_{\mathbf{u} \sim G} [\ln \pi(\mathbf{u})]$ is independent of \mathbf{u} (i.e., it is a constant), from the exponentiation of both sides of (D2) it follows that $\pi(\mathbf{v}) \propto e^{-\mathcal{H}(\mathbf{v})}$ holds for $N = 2$.

Next, assuming the following identity holds

$$\begin{aligned} \mathcal{H}(\mathbf{v}^*) &= - \sum_{n=1}^{N-1} \sum_{i_1=1}^{N-n} \sum_{i_2=i_1+1}^{N-n+1} \dots \sum_{i_n=i_{n-1}+1}^{N-1} \sum_{K \subseteq [n]} (-1)^{n-|K|} \mathbb{E}_{\mathbf{u}^* \sim G^*} [\ln \pi^*(\mathbf{u}^*) | u_{i_k}^* = v_{i_k}^* : k \in K] \\ &= -\ln \pi^*(\mathbf{v}^*) + \mathbb{E}_{\mathbf{u}^* \sim G^*} [\ln \pi^*(\mathbf{u}^*)], \end{aligned} \quad (\text{D3})$$

for any probability mass π^* defined over a dimension $N - 1$ sample space Ω^* , we will prove that it also holds when the dimension of the sample space is N . First, Let us separate couplings that include the site $i_1 = 1$ from those that do not in (D1)

$$\begin{aligned} \mathcal{H}(\mathbf{v}) &= - \sum_{n=1}^N \sum_{i_1=1}^1 \sum_{i_2=2}^{N-n+2} \dots \sum_{i_n=i_{n-1}+1}^N \sum_{K \subseteq [n]} (-1)^{n-|K|} \mathbb{E}_{\mathbf{u} \sim G} [\ln \pi(\mathbf{u}) | u_{i_k} = v_{i_k} : k \in K] \\ &\quad - \sum_{n=1}^{N-1} \sum_{i_1=2}^{N-n+1} \sum_{i_2=i_1+1}^{N-n+2} \dots \sum_{i_n=i_{n-1}+1}^N \sum_{K \subseteq [n]} (-1)^{n-|K|} \mathbb{E}_{\mathbf{u} \sim G} [\ln \pi(\mathbf{u}) | u_{i_k} = v_{i_k} : k \in K]. \end{aligned} \quad (\text{D4})$$

Besides, from coupling definition (11) we note that

$$\begin{aligned} J_{i_1 \dots i_n}^{\mu_1 \dots \mu_n} \delta_{\mu_1}^{v_{i_1}} \dots \delta_{\mu_n}^{v_{i_n}} &= \sum_{K \subseteq [n]} (-1)^{n-|K|} \mathbb{E}_{\mathbf{u} \sim G} [\ln \pi(\mathbf{u}) | u_{i_k} = v_{i_k} : k \in K] \\ &= \sum_{K \subseteq [n] \setminus \{1\}} (-1)^{n-|K|} \left[\mathbb{E}_{\mathbf{u} \sim G} [\ln \pi(\mathbf{u}) | u_{i_k} = v_{i_k} : k \in K] - \mathbb{E}_{\mathbf{u} \sim G} [\ln \pi(\mathbf{u}) | u_{i_k} = v_{i_k} : k \in K \cup \{1\}] \right]. \end{aligned} \quad (\text{D5})$$

Replacing (D5) in the first line r.h.s. of (D4) line gives

$$\begin{aligned}
& - \sum_{n=1}^N \sum_{i_1=1}^1 \sum_{i_2=2}^{N-n+2} \dots \sum_{i_n=i_{n-1}+1}^N \sum_{K \subseteq [n] \setminus \{1\}} (-1)^{n-|K|} \left[\mathbb{E}_{\mathbf{u} \sim G} [\ln \pi(\mathbf{u}) | u_{i_k} = v_{i_k} : k \in K] - \mathbb{E}_{\mathbf{u} \sim G} [\ln \pi(\mathbf{u}) | u_{i_k} = v_{i_k} : k \in K \cup \{1\}] \right] \\
& = \sum_{n=0}^{N-1} \sum_{i_1=2}^{N-n+1} \dots \sum_{i_n=i_{n-1}+1}^N \sum_{K \subseteq [n]} (-1)^{n-|K|} \left[\mathbb{E}_{\mathbf{u} \sim G} [\ln \pi(\mathbf{u}) | u_{i_k} = v_{i_k} : k \in K] - \mathbb{E}_{\mathbf{u}^* \sim G^*} [\ln \pi(v_1, \mathbf{u}^*) | u_{i_k} = v_{i_k} : k \in K] \right], \quad (\text{D6})
\end{aligned}$$

with $\mathbf{u}^* \stackrel{\text{def}}{=} (u_2, \dots, u_N)$, hence $\pi(v_1, \mathbf{u}^*) = \pi(v_1, u_2, \dots, u_N)$. Additionally, in (D6) we denoted by G^* the corresponding marginal probability measure of G for $\mathbf{u}^* \in \Omega^*$. Substituting (D6) in the first line of (D4) gives

$$\begin{aligned}
\mathcal{H}(\mathbf{v}) & = - \sum_{n=1}^{N-1} \sum_{i_1=2}^{N-n+1} \dots \sum_{i_n=i_{n-1}+1}^N \sum_{K \subseteq [n]} (-1)^{n-|K|} \mathbb{E}_{\mathbf{u}^* \sim G^*} [\ln \pi(v_1, \mathbf{u}^*) | u_{i_k}^* = v_{i_k} : k \in K] \\
& \quad + \mathbb{E}_{\mathbf{u} \sim G} [\ln \pi(\mathbf{u})] - \mathbb{E}_{\mathbf{u}^* \sim G^*} [\ln \pi(v_1, \mathbf{u}^*)] \quad (\text{D7})
\end{aligned}$$

Using the induction hypothesis (D3) in the first line of r.h.s. of (D7) readily verifies that $\mathcal{H}(\mathbf{v}) = -\ln \pi(\mathbf{v}) + \mathbb{E}_{\mathbf{u} \sim G} [\ln \pi(\mathbf{u})]$ holds. \blacksquare

We remark that the gauge freedom above manifests in the arbitrariness of the G choice to compute the couplings. Further, we can relate Eq. (11) with the more familiar gauge fixing conditions whenever the probability measure G is factorizable through the following theorem:

Theorem 2. Gauge Fixing. *Considering the effective couplings $J_{i_1 \dots i_n}^{\mu_1 \dots \mu_n}$ defined in Eq. (11), let g be the probability mass function of G such that $g(\mathbf{v}) = \prod_{i=1}^N g_i(v_i)$. Then, it follows that*

$$\sum_{\mu'} g_{i_n}(\mu') J_{i_1 \dots i_n}^{\mu_1 \dots \mu'} = 0 \quad (\text{D8})$$

for all i_1, \dots, i_n and μ_1, \dots, μ_n .

Proof. By simply replacing Eq. (11) in (D8) we can obtain

$$\begin{aligned}
\sum_{\mu'} g_{i_n}(\mu') J_{i_1 \dots i_n}^{\mu_1 \dots \mu'} & = \sum_{\mu'} g_{i_n}(\mu') \sum_{K \subseteq [n]} (-1)^{n-|K|} \mathbb{E}_{\mathbf{u} \sim G} [\ln \pi(\mathbf{u}) | u_{i_k} = \mu_k : k \in K] \quad (\text{with } \mu_n = \mu') \\
& = \sum_{\mu'} g_{i_n}(\mu') \sum_{K \subseteq [n-1]} (-1)^{n-|K|} \left[\mathbb{E}_{\mathbf{u} \sim G} [\ln \pi(u_1, \dots, u_{i_n}, \dots, u_N) | u_{i_k} = \mu_k : k \in K] \right. \\
& \quad \left. - \mathbb{E}_{\mathbf{u} \sim G} [\ln \pi(u_1, \dots, \mu', \dots, u_N) | u_{i_k} = \mu_k : k \in K] \right] \\
& = \sum_{K \subseteq [n-1]} (-1)^{n-|K|} \left[\sum_{u_1} g_1(u_1) \dots \sum_{u_{i_n}} g_{i_n}(u_{i_n}) \dots \sum_{u_N} g_N(u_N) [\ln \pi(u_1, \dots, u_{i_n}, \dots, u_N) | u_{i_k} = \mu_k : k \in K] \right. \\
& \quad \left. - \sum_{\mu'} g_{i_n}(\mu') \sum_{u_1} g_1(u_1) \dots \sum_{u_N} g_N(u_N) [\ln \pi(u_1, \dots, \mu', \dots, u_N) | u_{i_k} = \mu_k : k \in K] \right] = 0.
\end{aligned}$$

According to the above theorem, using a probability mass function in the coupling definition in Eq. (11) such that $g_i(u_i) = \delta_q^{u_i}$ or $g_i(u_i) = q^{-1}$ leads automatically to fix the lattice gas (Eq. (7)) or zero-sum (Eq. (8)) gauges, respectively.

Finally, to provide a strong argument for why low-order expansions of an effective Hamiltonian $\mathcal{H}^{(L)}(\mathbf{v})$ (with $N > L$) in the zero-sum gauge more accurately represent the full Hamiltonian $\mathcal{H}(\mathbf{v})$ than that in the lattice gas gauge, let us introduce the following theorem:

Theorem 3. *Let G be a probability measure defined over Ω and \mathcal{L}_G be the error function between an effective Hamiltonian with arbitrary high-order interactions \mathcal{H} and a truncated version keeping up to L -th order interactions $\mathcal{H}^{(L)}$ defined by*

$$\mathcal{L}_G \equiv \mathbb{E}_{\mathbf{v} \sim G} \left[\left(\mathcal{H}(\mathbf{v}) - \mathcal{H}^{(L)}(\mathbf{v}) \right)^2 \right]. \quad (\text{D9})$$

If G is factorizable then \mathcal{L}_G is minimized when $\mathcal{H}^{(L)}(\mathbf{v})$ is written in the gauge induced by G .

Proof. Since \mathcal{L}_G is convex, in this case, it is enough to prove that $\partial\mathcal{L}_G/\partial J_{i_1\dots j_l}^{\mu_1\dots\mu_l} = 0$, for every coupling parameter $J_{i_1\dots j_l}^{\mu_1\dots\mu_l}$ of $\mathcal{H}^{(L)}$, where $L \geq l$, when these are written in the gauge induced by G . By applying the chain rule, one can obtain

$$\frac{\partial\mathcal{L}_G}{\partial J_{i_1\dots j_l}^{\mu_1\dots\mu_l}} = 2 \mathbb{E}_{\mathbf{v} \sim G} \left[\left(\mathcal{H}(\mathbf{v}) - \mathcal{H}^{(L)}(\mathbf{v}) \right) \delta_{\mu_1}^{v_{i_1}} \dots \delta_{\mu_l}^{v_{i_l}} \right], \quad (\text{D10})$$

where we used $\partial\mathcal{H}^{(L)}(\mathbf{v})/\partial J_{i_1\dots j_l}^{\mu_1\dots\mu_l} = \delta_{\mu_1}^{v_{i_1}} \dots \delta_{\mu_l}^{v_{i_l}}$. Rewriting the difference between Hamiltonians inside the brackets using the gauge induced by G in (D10) gives

$$\begin{aligned} \frac{\partial\mathcal{L}_G}{\partial J_{i_1\dots j_l}^{\mu_1\dots\mu_l}} &= -2 \mathbb{E}_{\mathbf{v} \sim G} \left[\left(\sum_{n=L+1}^N \sum_{j_1=1}^{N-n+1} \sum_{j_2=j_1+1}^{N-n+2} \dots \sum_{j_n=j_{n-1}+1}^N J_{j_1\dots j_n}^{v_{j_1}\dots v_{j_n}} \right) \delta_{\mu_1}^{v_{i_1}} \dots \delta_{\mu_l}^{v_{i_l}} \right] \\ &= -2 \sum_{v_{i_1}} g_{i_1}(v_{i_1}) \dots \sum_{v_{i_l}} g_{i_l}(v_{i_l}) \sum_{v_{i_{l+1}}} g_{i_{l+1}}(v_{i_{l+1}}) \dots \sum_{v_N} g_{i_N}(v_{i_N}) \left[\left(\sum_{n=L+1}^N \sum_{j_1=1}^{N-n+1} \sum_{j_2=j_1+1}^{N-n+2} \dots \sum_{j_n=j_{n-1}+1}^N J_{j_1\dots j_n}^{v_{j_1}\dots v_{j_n}} \right) \delta_{\mu_1}^{v_{i_1}} \dots \delta_{\mu_l}^{v_{i_l}} \right] \\ &= -2 \sum_{v_{i_{l+1}}} g_{i_{l+1}}(v_{i_{l+1}}) \dots \sum_{v_N} g_{i_N}(v_{i_N}) \left[\sum_{n=L+1}^N \sum_{j_1=1}^{N-n+1} \sum_{j_2=j_1+1}^{N-n+2} \dots \sum_{j_n=j_{n-1}+1}^N J_{j_1\dots j_n}^{v_{j_1}\dots v_{j_n}} \Big|_{v_{i_1}=\mu_1, \dots, v_{i_l}=\mu_l} \right]. \quad (\text{D11}) \end{aligned}$$

Since $n \geq L+1 > L \geq l$, we note in the above that there is at least one free site j_k in every multi-body coupling $J_{j_1\dots j_n}^{v_{j_1}\dots v_{j_n}}$ over which a sum $\sum_{v_{i_k}} g_{i_k}(v_{i_k}) J_{j_1\dots j_n}^{v_{j_1}\dots v_{j_n}}$ is carried out. Thus, the theorem 2 leads automatically to the r.h.s. of (D11) to vanish. \blacksquare

Therefore, the zero-sum minimizes \mathcal{L}_G when computed over all $\mathbf{v} \in \Omega$, giving every sequence the same weight. Such a fact was also proved by Feinauer et al. [18] when $L = 2$. Besides, the lattice-gas gauge minimizes this error when we compute over the sequence (q, \dots, q) .

Appendix E: Modified Blume-Capel Model

The Blume-Capel (BC) Model [41, 42], given by

$$\mathcal{H}(\mathbf{s}) = -J^{(2)} \sum_{\langle i,j \rangle} s_i s_j - D \sum_i s_i^2 - h \sum_i s_i, \quad (\text{E1})$$

where $\sigma_j \in \{-1, 0, 1\}$, can be seen as a spin-1 version of the Ising model. In Eq. (13), we introduced a modified version of the above model in which we set $D = h = 0$ and included three-wise couplings $J^{(3)}$. Considering the following Potts-like Hamiltonian

$$\mathcal{H}_{\mathcal{D}}(\mathbf{v}) = - \sum_{\langle i,j,k \rangle} \sum_{\mu,\nu,\xi} J_{ijk}^{\mu\nu\xi} \delta_{\mu}^{v_i} \delta_{\nu}^{v_j} \delta_{\xi}^{v_k} - \sum_{\langle i,j \rangle} \sum_{\mu,\nu} J_{ij}^{\mu\nu} \delta_{\mu}^{v_i} \delta_{\nu}^{v_j}, \quad (\text{E2})$$

we obtain the same model defined by (13) assuming the following correspondence between \mathbf{s} and \mathbf{v}

$$\begin{aligned} s_i = -1 &\leftrightarrow v_i = 1 \\ s_i = 1 &\leftrightarrow v_i = 2 \\ s_i = 0 &\leftrightarrow v_i = 3, \end{aligned}$$

and defining the pairwise and three-wise parameters of the Potts model for i, j , and k neighbor sites as

$$\begin{aligned} J_{ij}^{\mu\nu} &= \begin{cases} J & \text{if } \mu = \nu \text{ and } \{\mu, \nu\} \not\supseteq 3 \\ -J & \text{if } \mu \neq \nu \text{ and } \{\mu, \nu\} \not\supseteq 3 \text{ and,} \\ 0 & \text{if } \{\mu, \nu\} \supseteq 3, \end{cases} \\ J_{ijk}^{\mu\nu\xi} &= \begin{cases} J & \text{if } \{\mu, \nu, \xi\} \not\supseteq 3 \text{ and } \mu + \nu + \xi \text{ even,} \\ -J & \text{if } \{\mu, \nu, \xi\} \not\supseteq 3 \text{ and } \mu + \nu + \xi \text{ odd,} \\ 0 & \text{if } \{\mu, \nu, \xi\} \supseteq 3, \end{cases} \end{aligned}$$

where $\mu, \nu, \xi \in \{1, 2, 3\}$. Finally, we emphasize that in Fig. 2A, we showed the mean and standard deviation of the aggregated inferred couplings defined as

$$\overline{J_{ij}^{(2)}} \stackrel{\text{def}}{=} \frac{1}{4} \{ J_{ij}^{22} - J_{ij}^{21} - J_{ij}^{12} + J_{ij}^{11} \} + \sum_{\{\mu, \nu\} \cap \{3\} \neq \emptyset} J_{ij}^{\mu\nu}, \text{ and}$$

$$\overline{J_{ijk}^{(3)}} \stackrel{\text{def}}{=} \frac{1}{4} \{ J_{ijk}^{222} - J_{ijk}^{221} - J_{ijk}^{212} - J_{ijk}^{122} + J_{ijk}^{112} + J_{ijk}^{121} + J_{ijk}^{211} - J_{ijk}^{111} \} + \sum_{\{\mu, \nu, \xi\} \cap \{3\} \neq \emptyset} J_{ijk}^{\mu\nu\xi}.$$

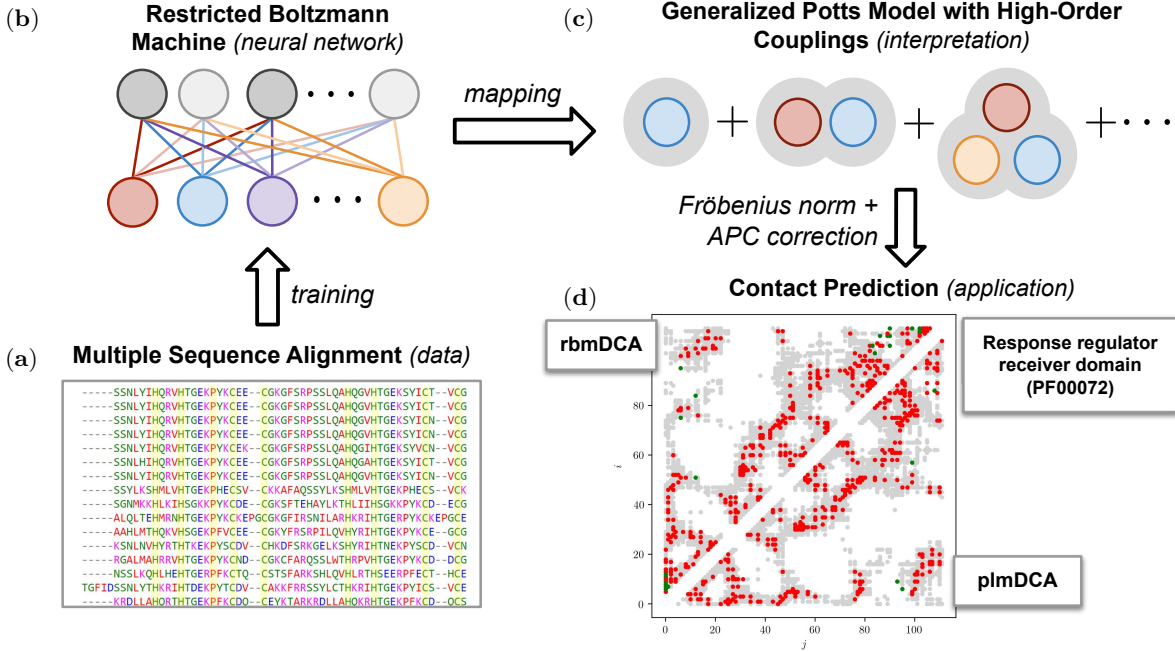


FIG. 5. **Epistatic coupling extraction from Neural Networks.** The above sketches the protein contact prediction task from Multiple Sequence Alignment (MSA) as an example of how mapping neural networks onto the Potts Model improves interpretability. The above *pipeline* depicts, first, the training of the neural network (e.g., an RBM) (b) with data (e.g., MSA) (a). Then, the trained model (b) is mapped onto a Potts-like model (c) using the mapping provided by this work. Finally, parameters of (b) can be used to predict epistatic contacts in the tertiary structure of the protein. (d) shows the contact prediction obtained for the Response Regulator Receiver Domain family (Pfam entry: PF00072), where light-gray dots are the contacts of the protein, red dots are true positives, and green dots are false positives. We showed the prediction obtained with our RBM-based inference (rbmDCA) in the upper-left part of the matrix, while the prediction obtained with the well-established pseudo-likelihood inference (plmDCA) is shown in the lower-right part.

Appendix F: Direct Coupling Analysis

A homologous protein family consists of a group of proteins that share similar biological functions, three-dimensional structures, and a common evolutionary origin. Given a collection of M homologous protein sequences, these can be arranged into a matrix with M rows and N columns, known as a *Multiple Sequence Alignment* (MSA). Constructing an MSA from large ensembles of biological sequences is a complex task, and a detailed discussion falls beyond the scope of this manuscript (for a comprehensive treatment, see the classic reference [43]).

Each position in an MSA typically assumes one of 21 possible states, corresponding to the 20 standard amino acids and a *gap* that accounts for insertion or deletion mutations occurring throughout evolutionary history. While sequence variation within each column naturally arises from evolution, some positions exhibit significantly less variability due to *stabilizing selection*^{*}, which preserves critical functional or structural sites, such as a protein's binding or active site.

In addition to conserved sites, certain pairs of distant columns exhibit correlated mutations, where a change in another systematically accompanies a shift in one position. These *epistatic* interactions suggest structural or functional

constraints, often indicating physical contacts in the protein’s tertiary structure. Such co-evolving sites arise because interacting amino acids can be replaced by another pair that maintains similar physico-chemical interactions, thereby preserving the protein’s overall structure and function.

Constructing a maximum entropy model to capture the statistical properties of conserved positions and pairwise epistatic contacts in MSA data naturally leads to the Potts model [11]:

$$H(\mathbf{v}) = - \sum_{1 \leq i < j \leq N} \sum_{\mu, \nu} J_{ij}^{\mu\nu} \delta_{\mu}^{v_i} \delta_{\nu}^{v_j} - \sum_{i, \mu} H_i^{\mu} \delta_{\mu}^{v_i}, \quad (\text{F1})$$

where a strong field H_i^{μ} in any state μ indicates a conserved site in position i and significantly large epistatic couplings values $J_{ij}^{\mu\nu}$ suggest contact between sites i and j . The inference of the parameters of (F1) from MSA data is normally referred as the *Direct Coupling Analysis* (DCA). Existing DCA methods employ approaches such as pseudo-likelihood maximization [34, 35], Boltzmann machine learning [36, 37], and auto-regressive models [33], among others. This work introduces a new method to this framework: RBM-DCA.

As is standard in DCA analysis [11], after inferring the epistatic couplings in Eq. (F1), the *coupling strength* between two sites i and j is computed as the Frobenius norm of the corresponding coupling matrix, given by:

$$F_{ij}^{(2)} = \sqrt{\sum_{\mu, \nu} (J_{ij}^{\mu\nu})^2}. \quad (\text{F2})$$

Then, we can achieve an ever better contact prediction performance by implementing the *average-product correction* (APC) [44]:

$$F_{ij}^{\text{APC}} = F_{ij}^{(2)} - \frac{\sum_k F_{ik}^{(2)} \sum_k F_{kj}^{(2)}}{\sum_{k,l} F_{kl}^{(2)}}, \quad (\text{F3})$$

which intends to minimize any background noise [45, 46].

In the figure 5, we showed the general pipeline followed to conduct a contact prediction from MSA. The MSA data we used correspond to the companion data provided in Ref. [33] for the PF00072 protein family, including structural data of a tertiary structure in this family.

The training code used has been incorporated into GitHub:DsysDML/rbms, a Python-based library for RBM training. Besides, the coupling extraction and contact routines were implemented in the public repository GitHub:DsysDML/couplings_inference. One of our most significant practical achievements was implementing a parallelization algorithm that makes the computation of high-order couplings achievable; in the following, we read typical computation times obtained for the model trained with PF00072 MSA data:

TABLE I. Typical computation times obtained for a system with $N_v = 112$, $N_h = 1000$ and $q = 21$.

computation	time (ms)
fields ($q \times N_v$)	15.00 ± 0.04
2-body couplings ($q \times q$)	4.29 ± 0.03
3-body couplings ($q \times q \times q$)	52.5 ± 0.34

The above computations were done on an NVIDIA Geforce RTX 3090 graphic card with 24 GB memory. All external fields can be computed in parallel, while 2-body and 3-body couplings were calculated for each pair or triad sequentially. The total time required to compute all the 2-body and 3-body couplings was approximately 27s and 3h 20min, respectively.